

MDPI

Article

Investigation of the Flow Behavior of Air-Cooling Ti-6Al-4V Alloy after Superplastic Forming

Xiaoning Han 1,*, Junzhou Yang 2, Jinshan Li 1,3,* and Jianjun Wu 2,*

- State Key Laboratory of Solidification Processing, Northwestern Polytechnical University, Xi'an 710072, China
- School of Mechanical Engineering, Northwestern Polytechnical University, Xi'an 710072, China; yjz@mail.nwpu.edu.cn
- ³ Chongging Innovation Center, Northwestern Polytechnical University, Chongging 401135, China
- * Correspondence: hxn10102@126.com (X.H.); ljsh@nwpu.edu.cn (J.L.); wujj@nwpu.edu.cn (J.W.)

Abstract: The flow behavior of Ti-6Al-4V alloy during the air-cooling process after superplastic forming (SPF) has been discussed. In high-temperature constant strain rate tensile tests, the selected temperatures were 930, 900, 800, 700, and 600 °C, and the initial strain rates were 10^{-2} , 10^{-3} , and 10^{-4} /s. The optimized deformation temperatures were $800\sim900$ °C and the strain rates were $10^{-4}\sim10^{-3}$ /s. Then, the evolutions of activation energy and deformation strain are also discussed, and the effects of dislocation density and deformation activation energy on flow behavior were consistent. In addition, unstable flow is mainly concentrated in the low-temperature and high strain-rate regions, and this is mainly caused by dynamic recrystallization (DRX). After the SPF process, the possibility of material damage gradually increases during the air-cooling process.

Keywords: superplastic forming; Ti-6Al-4V; air cooling; flow behavior



Citation: Han, X.; Yang, J.; Li, J.; Wu, J. Investigation of the Flow Behavior of Air-Cooling Ti-6Al-4V Alloy after Superplastic Forming. *Crystals* **2022**, *12*, 294. https://doi.org/10.3390/cryst12020294

Academic Editors: Antonio J. Gámez, Luis Garcia Barrachina, Vit Janik, Donato Sorgente and Vincent Velay

Received: 24 January 2022 Accepted: 15 February 2022 Published: 19 February 2022

Publisher's Note: MDPI stays neutral with regard to jurisdictional claims in published maps and institutional affiliations.



Copyright: © 2022 by the authors. Licensee MDPI, Basel, Switzerland. This article is an open access article distributed under the terms and conditions of the Creative Commons Attribution (CC BY) license (https://creativecommons.org/licenses/by/4.0/).

1. Introduction

Ti-6Al-4V alloy is a polycrystalline metal with two isomers: α-phase with hexagonal close-packed (HCP) structure and the β-phase with body-centered cubic (BCC) structure [1–3]. It has the following mechanical properties: (i) low density and high specific strength; (ii) high temperature resistance; and (iii) excellent corrosion resistance. So, it has been widely used in aircraft, missiles, ships, automobiles, petroleum, chemical industry, biomedicine, and other fields [4–6]. For titanium parts with complex structures, superplastic forming (SPF) is usually employed in aerospace industries [7–10]. The superplasticity of Ti-6Al-4V alloy refers to the properties that materials can achieve of great elongation without fracture within a certain range of temperatures (about 900 °C) and strain rates $(10^{-4} \sim 10^{-2}/s)$ [11,12]. The requirements of such high temperatures and low strain rates will lead to high costs. In addition, there is a contradiction between the large deformation and the serious thickness distribution caused by drastic strains. So, this research on superplasticity is still worth studying at present.

It has been recognized that the superplastic deformation is dominant by the grain boundary sliding (GBS), and the research focus is the accommodated mechanism of GBS [13]. Especially for Ti-6Al-4V alloy, diffusion-accommodated, dislocation-accommodated, and other accommodation mechanisms are still debated [14–16]. Another research focus is modifying the SPF process windows by controlling grain sizes [17,18] or other methods [19]. The flow behaviors of materials depend on different treatments, so the rheological behaviors of superplastic deformation and air cooling are due to the evolution of the microstructures. However, the research on this aspect is still insufficient.

It can be easily understood that superplastic forming is carried out at high temperatures, but the measurements of whether the forming part meets requirements are always performed at room temperatures. For the unqualified SPF parts, it is unreasonable to directly attribute the failure to the superplastic forming process; the air-cooling process of

Crystals **2022**, 12, 294 2 of 12

being taken out from the furnace to room condition after SPF may also decline qualities of products. Additionally, the structures of the inhomogeneity lead to the generation of temperature gradient during the cooling process, resulting in residual stress and residual deformation. For thin-walled hollow structures, research on the flow behavior during air cooling should not be ignored.

Thus, this paper investigates the flow behavior of Ti-6Al-4V alloy during the air cooling process after SPF. The article is divided into three parts: (i) the strain rate sensitivity factors; (ii) the deformation activation energies; and (iii) hot working process maps.

2. Materials and Methods

The material used in this study is a rolled sheet of 1mm thickness. Based on energy dispersive spectrometry (EDS), the chemical compositions of material in weight percent are obtained, as shown in Table 1. Figure 1 presents the initial microstructures by optical microscope (OM); the titanium consists of equiaxed α -phase grains and a small amount of β - phase grains.

Table 1. Chemical compositions of Ti-6Al-4V alloy.

Chemistry (wt.%)	Ti	Al	V	С
Ti-6Al-4V	88.31	5.59	4.85	1.25

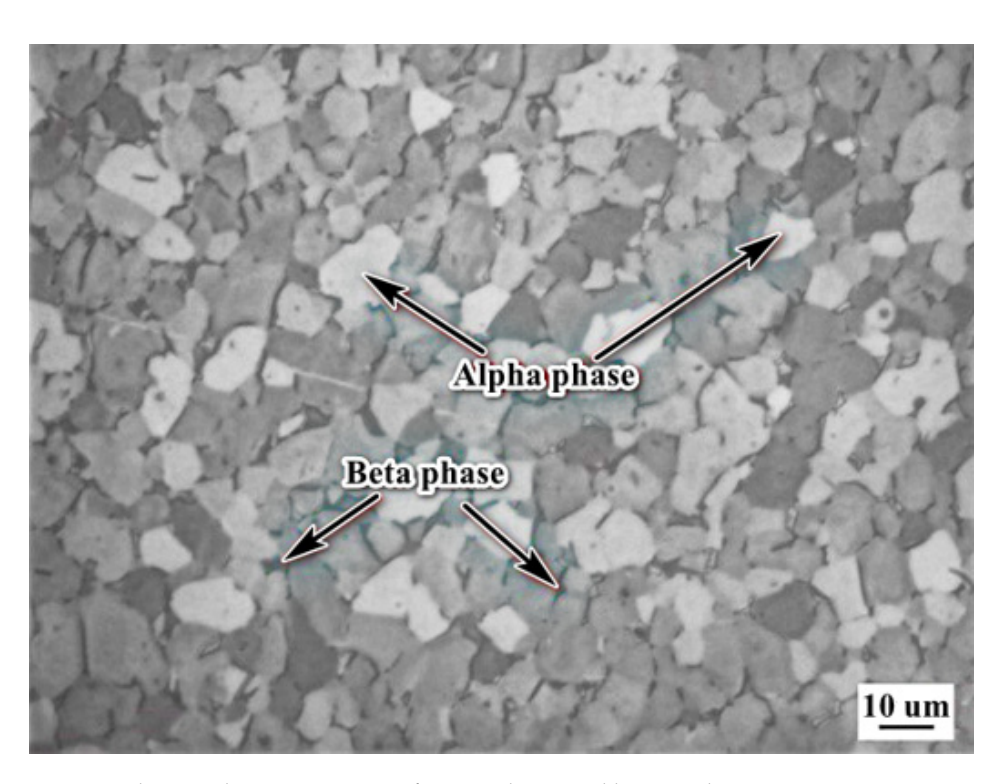


Figure 1. The initial microstructure of received material by OM observation.

High-temperature tensile tests were performed on a Shimazu Electronic Universal Testing Machine. The experimental specimens were cut by wire electrical discharge machining, and the dimensions are given in Figure 2. Before high-temperature stretching, all samples are polished with 1500# sandpapers to ensure good contacts between samples and thermocouples. Firstly, the sample was heated at a rate of 20 $^{\circ}$ C/min to 950 $^{\circ}$ C and held for 5 min. Next, air-cooling temperatures were carried out to 930, 900, 800, 700, and 600 $^{\circ}$ C and held for 10 min. High-temperature tensile tests were carried out at each temperature, with initial strain rates of 10^{-2} , 10^{-3} , and 10^{-4} /s.

Crystals **2022**, 12, 294 3 of 12

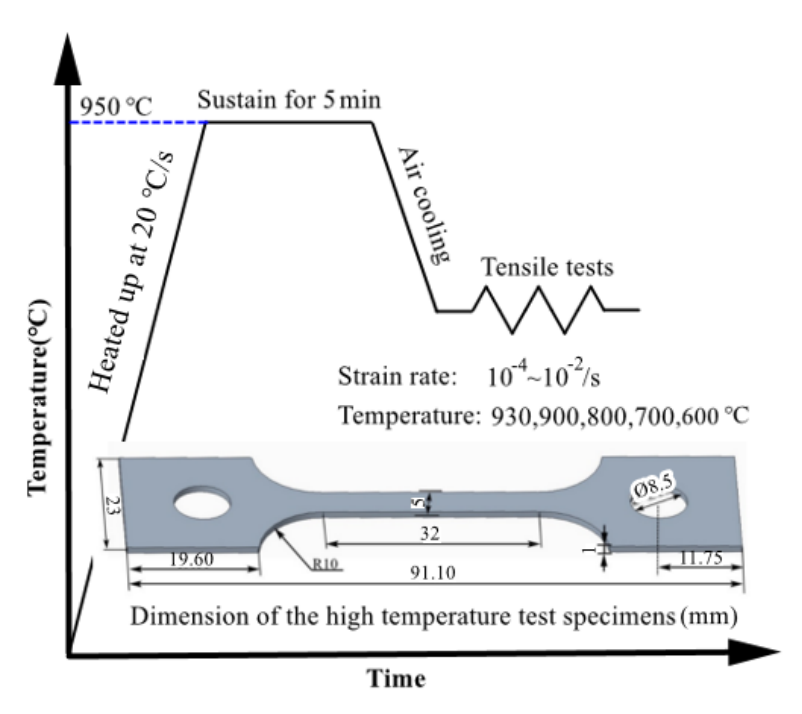


Figure 2. The dimensions of high-temperature tensile tests specimens and experiment process.

Electron back-scattered diffraction (EBSD) observations were performed to measure the evolutions of the grain size. The samples for microstructure observations were cut from the deformation zones of tensile specimens firstly. Each sample was hand polished with 240#, 320#, 1500#, 2500#, and 3000# sandpapers until the surface was flat and free of obvious scratches, and then all the samples were polished by ion beam figuring (IBF). The EBSD tests were carried out by ZEISS Gemini 500 Field Emission Scanning Electron Microscopy, and the results were analyzed by Channel 5 software.

3. Flow Behavior for Ti-6Al-4V Alloy during Air Cooling after SPF

3.1. Flow Stress Result of the Tensile Tests

It is difficult to measure the deformation strain with an extensometer when tensile testing at such high temperatures. In this paper, the load–displacement curves obtained are converted to the real stress and strain values based on Equation (1), and the results are listed in Table 2.

$$\begin{cases}
\sigma = \frac{F}{A_0} \left(1 + \frac{\Delta L}{L_0} \right) \\
\varepsilon = \ln \left(1 + \frac{\Delta L}{L_0} \right)
\end{cases}$$
(1)

where σ is the true stress, ε is the true strain, F is the load applied to the crossheads, A_0 is the initial cross-sectional area of the specimen, ΔL is the elongation of the specimen, which takes into account the deformation of the pinholes, and L_0 is the gauge of the specimen.

Table 2. The selected flow stresses of tensile testing for Ti-6Al-4V alloy after air cooling (MPa).

Strain	Strain Rate (s ⁻¹)	Tensile Test Temperature (°C)				
		600	700	800	900	930
0.10	$ \begin{array}{r} 10^{-4} \\ 10^{-3} \\ 10^{-2} \end{array} $	309.91 381.45 434.41	136.60 230.84 297.58	47.96 109.86 171.49	13.35 36.78 76.17	11.91 26.84 56.92
0.20	$ \begin{array}{r} 10^{-4} \\ 10^{-3} \\ 10^{-2} \end{array} $	281.71 371.60 431.44	121.77 208.56 281.87	42.60 94.88 154.45	13.69 33.06 64.93	13.33 24.94 48.07

Crystals **2022**, 12, 294 4 of 12

Table	2.	Cont
IdDIC	∠.	Con.

Strain	Strain Rate (s ⁻¹)	Tensile Test Temperature (°C)				
		600	700	800	900	930
0.30	10^{-4}	240.86	109.42	38.70	14.37	14.07
	10^{-3}	350.87	185.05	84.14	30.16	23.25
	10^{-2}	396.25	255.08	138.77	57.10	42.17
0.40	10^{-4}		99.95	35.79	14.57	14.81
	10^{-3}		162.43	75.73	27.65	21.84
	10^{-2}		221.93	124.60	50.86	37.47
0.50	10^{-4}		91.85	33.83	14.74	15.52
	10^{-3}		140.02	68.87	25.83	20.73
	10^{-2}			111.37	45.64	33.77
0.60	10^{-4}		84.11	31.88	14.55	15.78
	10^{-3}			63.04	24.38	19.82
	10^{-2}			98.51	40.60	30.43
0.70	10^{-4}		76.79	30.16	14.17	15.81
	10^{-3}			58.04	23.08	18.98
	10^{-2}			83.29	35.37	27.32

3.2. Strain Rate Sensitivity Factor

The flow stress of materials under high temperatures is highly sensitive to strain rates. During the deformation, the necking in specimens will always lead to the increase in strain rates, and stress strengthening occurs subsequently. Thus, the sections without neck contractions are more easily deformed than the neck contraction locations; thus, the above neck contraction stops and swims to other positions. The strain rate sensitivity factor m was first proposed by Backoften [20], which is always applied to describe the ability of materials to inhibit necking and its expansion:

$$m = \frac{dln\sigma}{dln\dot{\varepsilon}} \tag{2}$$

where ε is the strain rate, s⁻¹. The strain rate sensitivity factor is the slope of the linear fitting curve of $ln\sigma$ - $ln\varepsilon$. The calculation results of m when ε = 0.1, 0.2, 0.3, 0.5, 0.6, and 0.7 are shown in Figure 3.

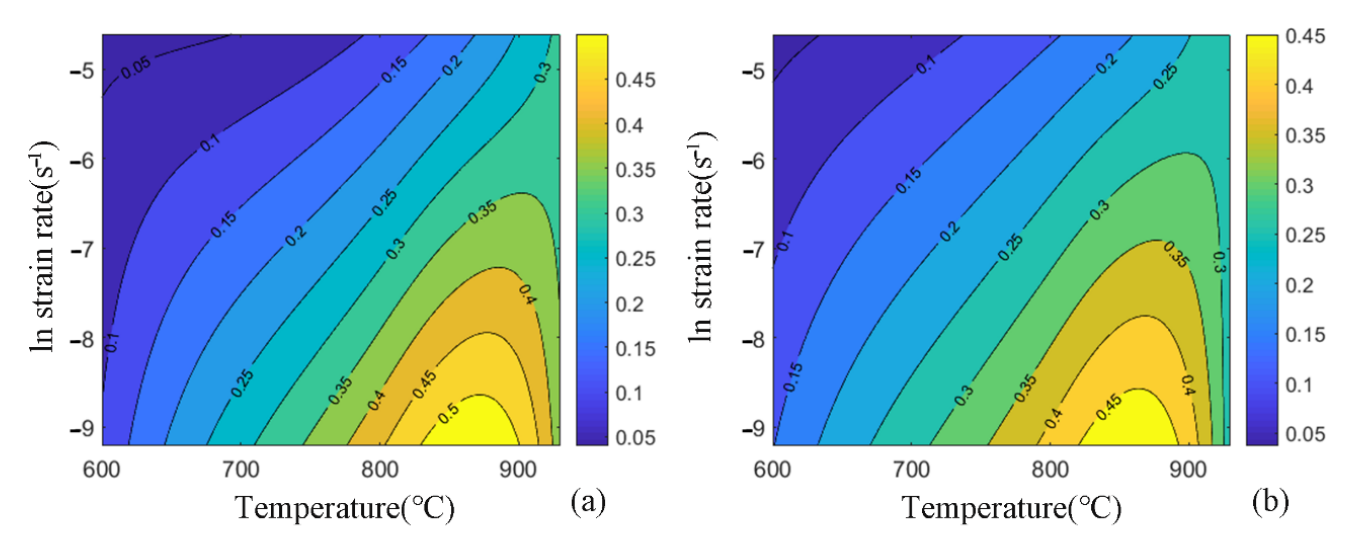


Figure 3. Cont.

Crystals **2022**, 12, 294 5 of 12

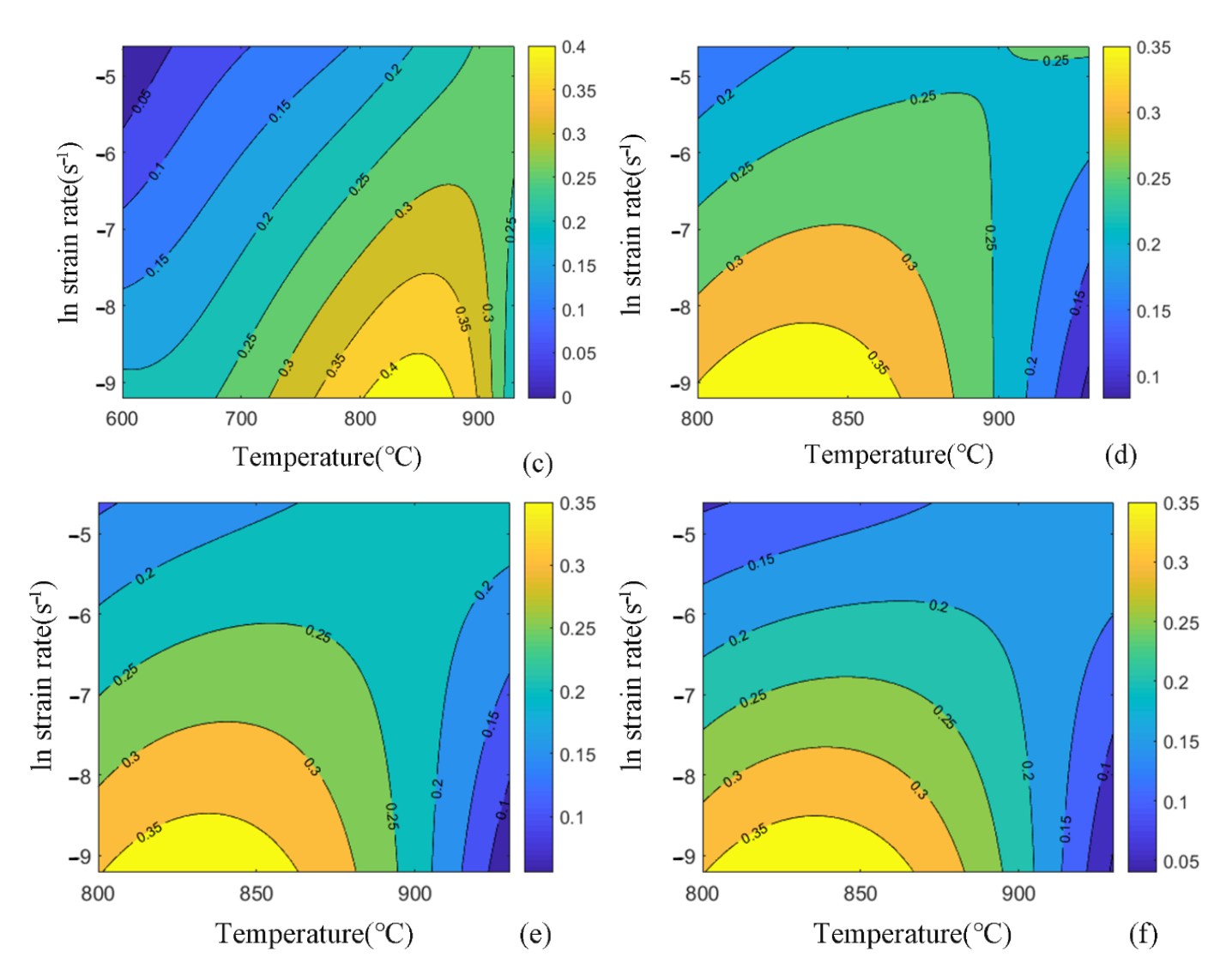


Figure 3. The strain rate sensitivity factors at different strains: (a) 0.1; (b) 0.2; (c) 0.3; (d) 0.5; (e) 0.6; (f) 0.7.

In this work, when stretching at low temperature, because the several sample fractures occur when the strain was greater than 0.4, only the m value between 800 °C~930 °C could be obtained. The distributions of strain rate sensitivity factors with temperatures and strain rates are similar under different strains:

- (i) In the cooling process after superplastic forming, m values are larger at high temperatures and low strain rates. The temperature regions of maximum m are concentrated between 800 °C~900 °C, and the strain rates are $10^{-4} \sim 10^{-3}$ /s. The interval is very similar to the results of superplastic deformation [21,22]; this is reasonable because both of them are thermal forming processes.
- (ii) The maximum values of strain rate sensitivity factors decrease gradually with the deformation, which indicates that the resistance of the material to necking decreases, which may be caused by the aggravation of the unstable flow of Ti-6Al-4V alloy. This issue will be discussed in detail in Section 4 of this paper.
- (iii) When the temperature is lower than 900 °C, the *m* values decrease with the increase in strain rates. The deformability of the material decreases at higher strain rates, which may be due to the microstructural defects, i.e., voids and cavitations [23,24]. Cavitation is inevitable in the process of material deformation. Cavitation is the accommodated mechanism for the high-temperature forming of titanium alloy, which affects the rheological behavior of the material and causes a decrease in flow stress.

Crystals **2022**, 12, 294 6 of 12

In addition, when the volume fraction of voids reaches a critical value, it is always considered to be directly related to the destruction of materials.

(iv) For the deformation at T > 900 $^{\circ}$ C, the strain rate sensitivity factors increase with the increase in strain rates at large stains, as are shown in Figure 3d–f. It can be inferred that within the range of higher temperatures and strain rates, there will still be another m concentration region. The 0.25 contour line in the upper right corner of (d) can be used as evidence for this inference. A hypothetical is proposed as an explanation for this phenomenon: when the material deforms at higher temperatures, the dislocations gain more energy. In addition, the dislocation velocities are positively correlated with the strain rates [25], so the dislocation movement becomes more intense at a high strain rate.

3.3. Deformation Activation Energy

The most prominent characteristic of high-temperature deformation is that the deformation process is controlled by the thermal activation process. Deformation activation energy represents the values of the energy barriers for atomic transition, and it can reflect the difficulty of plastic deformation of the material. When describing plastic deformation, the Arrhenius model is usually used to describe parameters related to temperature and rate. The mathematical expression is as follows:

$$\begin{cases}
Z = \dot{\varepsilon} \exp(Q/RT) \\
\dot{\varepsilon} = AF(\sigma) \exp(-Q/RT)
\end{cases}$$

$$F(\sigma) = \begin{cases}
\sigma^n & \alpha\sigma < 0.8 \\
\exp(\beta\sigma) & \alpha\sigma > 1.2 \\
[\sin h(\alpha\sigma)]^{\eta} & \text{for all stresses}
\end{cases}$$
(3)

where Z is the Zener–Hollomon parameter, which represents the comprehensive influence of temperature and strain rate on deformation; Q is the deformation active energy; R is the gas constant, R = 8.315 J/(mol·K); A, α , β , n, and η are material constants; and the expression of $F(\sigma)$ is different in various stress ranges [26]. The derivation of Equation (1) can be obtained:

$$\dot{\varepsilon} = A[\sin h(\alpha \sigma)]^{\eta} \exp(-Q/RT) \tag{4}$$

Taking the logarithm of Equation (4), as follows:

$$ln\dot{\varepsilon} = lnA + \eta ln[\sin h(\alpha\sigma)] - Q/RT \tag{5}$$

For the deformation at a constant temperature, $\dot{T} = 0$, differentiating Equation (5) concerning $ln[\sin h(\alpha\sigma)]$, the results hold

$$\eta = \frac{\partial ln\dot{\varepsilon}}{\partial \{ln[\sin h(\alpha\sigma)]\}} \tag{6}$$

Additionally, at a certain strain rate, $\dot{\varepsilon}=0$. Differentiating Equation (5) concerning the 1/T,

$$\begin{cases}
Q = R\eta K + I \\
K = \frac{\partial \{ln[\sin h(\alpha\sigma)]\}}{\partial (1/T)} \\
I = R \frac{\partial lnA}{\partial (1/T)} + R \frac{\partial \eta}{\partial (1/T)} - \frac{1}{T} \frac{\partial Q}{\partial (1/T)}
\end{cases}$$
(7)

The $ln[\sin h(\alpha\sigma)] - 1/T$ curves at $\varepsilon = 0.2$ for Ti-6Al-4V alloy during the air cooling after superplastic forming are shown in Figure 4. The values of I are small relative to the K, so the term I can be ignored, and $Q = R\eta K$.

Crystals **2022**, 12, 294 7 of 12

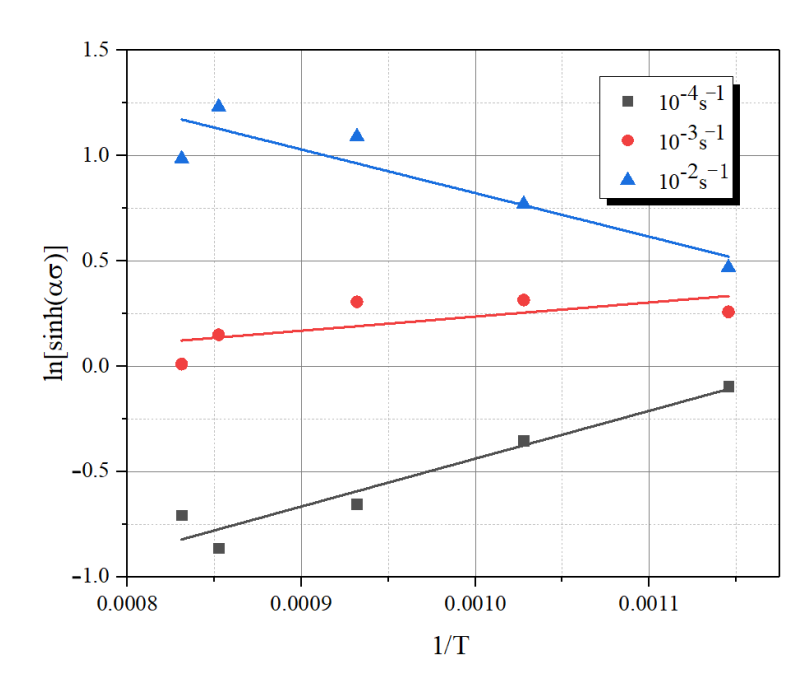


Figure 4. The fitting results of $ln[sinh(\alpha\sigma)]$ and 1/T.

In summary of Equations (6) and (7), the activation energy *Q* is given as:

$$Q = R \frac{\partial ln\dot{\varepsilon}}{\partial \{ln[\sin h(\alpha\sigma)]\}} \frac{\partial \{ln[\sin h(\alpha\sigma)]\}}{\partial (1/T)}$$
(8)

Figure 5 describes the activation energy calculated in this paper. The Q at the strain of 0.1, 0.2, and 0.3 for the deformation at 10^{-4} and 10^{-3} /s are discussed. For $\dot{\epsilon}=10^{-3}$ /s, the activation energy decreases with the increase in strain, and obvious flow softening can be obtained. However, for the deformation at the strain rate of 10^{-4} /s, the activation energy does not change significantly with the increase in strain. In this case, the material shows a typical strain hardening characteristic; that is, the flow stress increases with the increase in strain. When the stress increases to a critical value, it maintains stable flow stress. Traditionally, the softening phenomenon in the rheological behavior of materials is mainly caused by dynamic recovery (DRV) and dynamic recrystallization (DRX). While continuous dynamic recovery can eliminate strain hardening, the material maintains stable flow stress. Thus, DRX requires more energy than DRV, which usually results in more obvious stress softening [27]. Therefore, this suggests that the rheological behavior of materials at different temperatures and strain rates is related to the deformation activation energy of materials.

In terms of microstructure evolution, the deformation of materials is mainly controlled by dislocation movement [28]. Strain hardening is the result of the dislocation multiplication, and the larger dislocation density provides higher material strength. As the dislocation movement proceeds, the heterosign dislocations cancel each other, and the dislocation density decreases, resulting in stress softening. At higher temperatures, higher energy can be obtained in the dislocation movement process, so that the dislocation barrier can be overcome for climbing, and new softening behaviors can be generated, which is the reason for the low stress at high temperatures. In addition, when DRX occurs, the dislocations in the material are used to form subgrain dislocation walls, resulting in a reduction in the dislocation density. The effect of dislocation density and deformation activation energy on rheological behavior is consistent. Therefore, it can be considered that the dislocation motion is the main reason for the evolution of deformation activation energy of Ti-6Al-4V during hot deformation.

Crystals **2022**, 12, 294 8 of 12

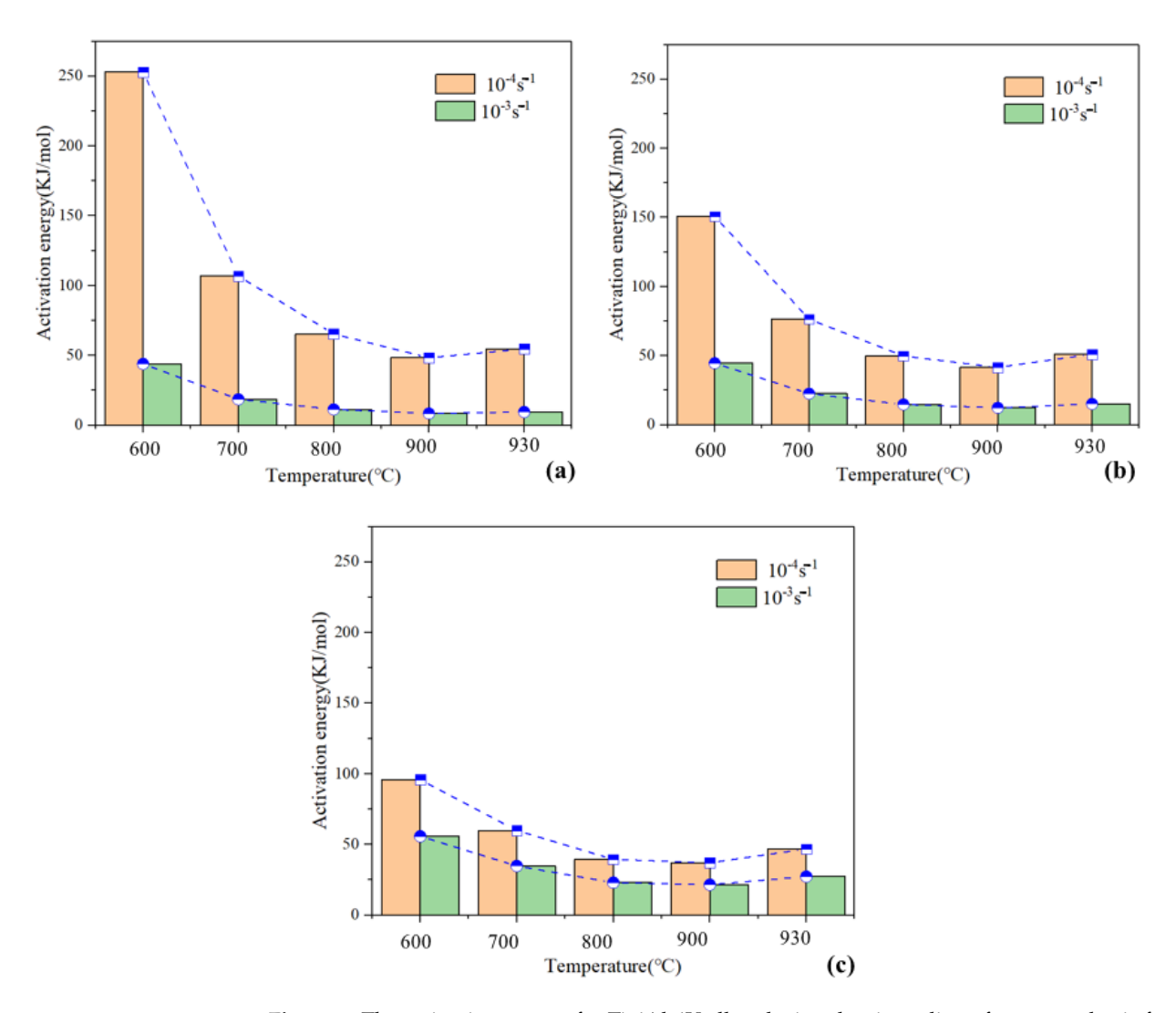


Figure 5. The activation energy for Ti-6Al-4V alloy during the sir cooling after superplastic forming: **(a)** 0.1; **(b)** 0.2; and **(c)** 0.3.

4. Process Maps for Ti-6Al-4V Alloy at Air Cooling Process

4.1. The Theory of Stable Flows

There are two kinds of fracture modes of materials during tensile deformation: necking and non-necking [29,30]. When the material has unstable flow, the first occurrence is necking, and then necking gradually transfer to fracture. In addition, for fractures without necking, the accumulation of voids is often observed at the fracture zone. The strain rate is small in this paper, and it is believed that the influence of void is small, focusing on the influence law of unstable flow. Based on the dynamic materials model (DMM) by Prasad [31], absorbing energy in the process of plastic flow P contributes in two main aspects: one is the plastic deformation energy dissipation $G = \int_0^{\varepsilon} \varepsilon d\sigma$; the other is due to the microstructure evolution and the dissipation of energy $J = \int_0^{\sigma} \varepsilon d\sigma$. Therefore, according to the definition, the energy dissipation rate (η) is expressed as:

$$\eta = \frac{P - G}{J_{max}} = \frac{2\left(\sigma\dot{\varepsilon} - \int_0^{\dot{\varepsilon}} \sigma d\dot{\varepsilon}\right)}{\sigma\dot{\varepsilon}} = \frac{2m}{m+1} \tag{9}$$

Crystals **2022**, 12, 294 9 of 12

Ziegler thinks that if the system has a plastic deformation of internal dissipation function D with strain rated $\frac{dD}{d\hat{\epsilon}} < \frac{D}{\hat{\epsilon}}$, then the system is unstable. Through sorting, the unsteady parameter ξ can be expressed as follows:

$$\xi = \frac{\partial lnD}{\partial ln\dot{\varepsilon}} - 1 = \frac{\partial ln\left(\frac{m}{m+1}\right)}{\partial ln\dot{\varepsilon}} + m < 0 \tag{10}$$

4.2. Hot Working Process Maps

According to the above calculation method, the energy dissipation rate η is calculated at each deformation temperature, and the energy dissipation rate under different deformation temperatures, strain rates, and strains can be obtained to form the energy dissipation curve. Equation (10) can be used to calculate the corresponding deformation temperature, strain rate, and the unsteady parameter ξ under strain. With the deformation temperature and strain rate as coordinates, the unsteady surface diagram under different strains can be obtained. Taking the deformation temperature and strain rate as coordinates, the energy dissipation rate surface and the unstable surface under different strains are constructed, and the two surface graphs are superimposed to form the hot working maps, as shown in Figure 6.

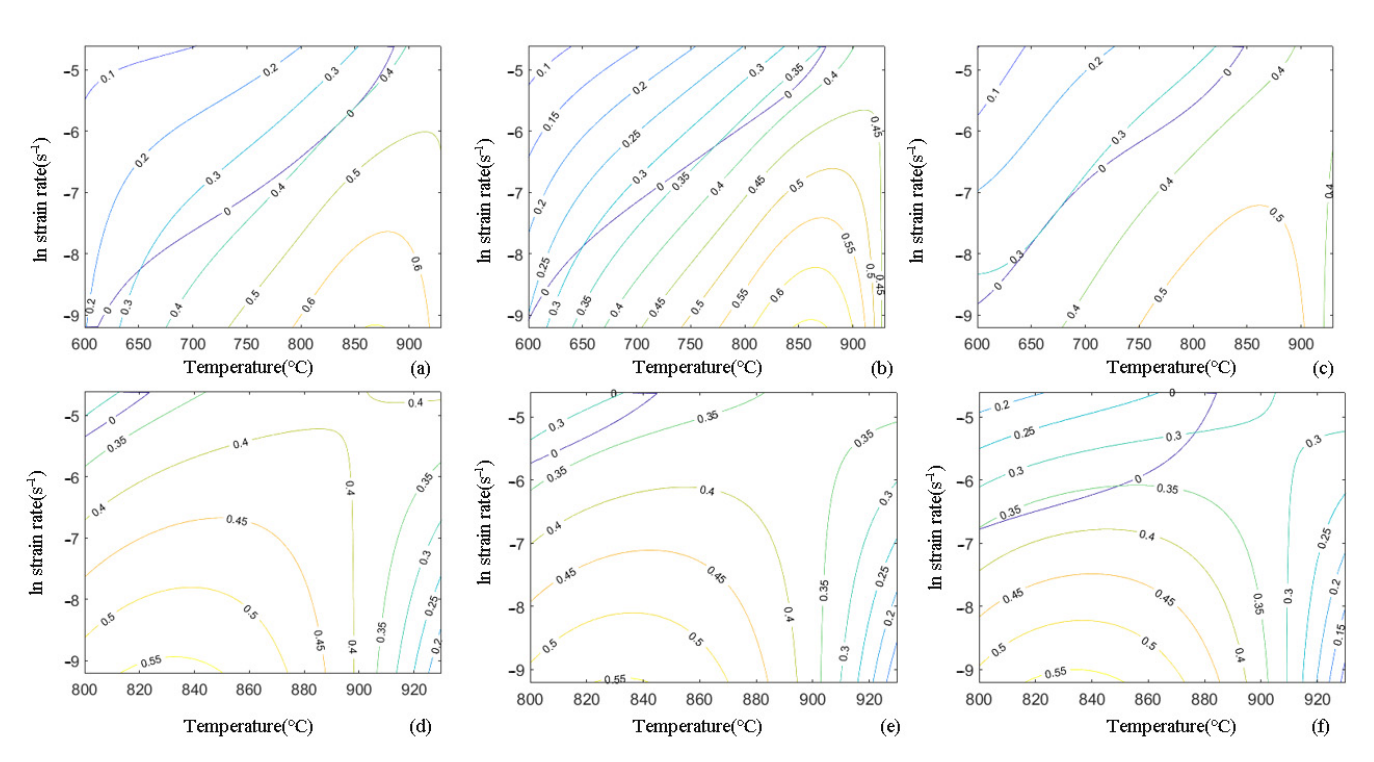


Figure 6. The processing map for Ti-6Al-4V alloy during the air cooling after superplastic forming: (a) 0.1; (b) 0.2; (c) 0.3; (d) 0.5; (e) 0.6; and (f) 0.7.

The peak area of the energy dissipation rate is basically: $800 \sim 900 \, ^{\circ}\text{C}$, $10^{-5} \sim 10^{-4}/\text{s}$. Additionally, the larger the strain, the smaller values of η . The process parameters corresponding to the peak value of energy dissipation rate are the best process parameters for air-cooling deformation after superplastic forming of Ti-6Al-4V alloy in the range of the test in this paper. The lower the energy dissipation rate is, the worse the deformation ability of the material is, and the more easily the failure phenomenon occurs in the air-cooling process.

The unstable flow is possible to occur at the low-temperature and high strain-rate regions, which is consistent with the material can achieve greater elongation at high temperature and low strain rate. Thus, in the process of cooling from 950 °C to 600 °C, the possibility of material damage gradually increases. In addition, the boundary line of the

Crystals **2022**, 12, 294 10 of 12

material stable flow is concentrated in the area of the energy dissipation rate between 0.3 and 0.4. Therefore, it can be considered that when the energy dissipation rate is less than 0.3, ξ < 0, the material will have an unstable flow.

4.3. The Microstructure Evolution during the Air-Cooling Process

In Figure 7, despite the EBSD inverse pole figures (IPF) for Ti-6Al-4V alloy during the air cooling process from 930 to 600 °C, the strain rate is 10^{-4} and 10^{-2} /s, respectively. When $\dot{\varepsilon}=10^{-2}$ /s, the grains become finer, and the volume fractions of DRX are larger as the temperature decreases. Thus, it is more and more obvious that DRX is responsible for the unstable flow stress, and this conclusion is obtained in the literature [21,32]. For Figure 7d–f, the only difference is that DRX just occurs at lower temperatures than that of 10^{-2} /s, so the material has better flow stability at low strain rates. Therefore, the cooling rates should be controlled as much as possible to ensure that the material has suitable strain rates during the air-cooling process.

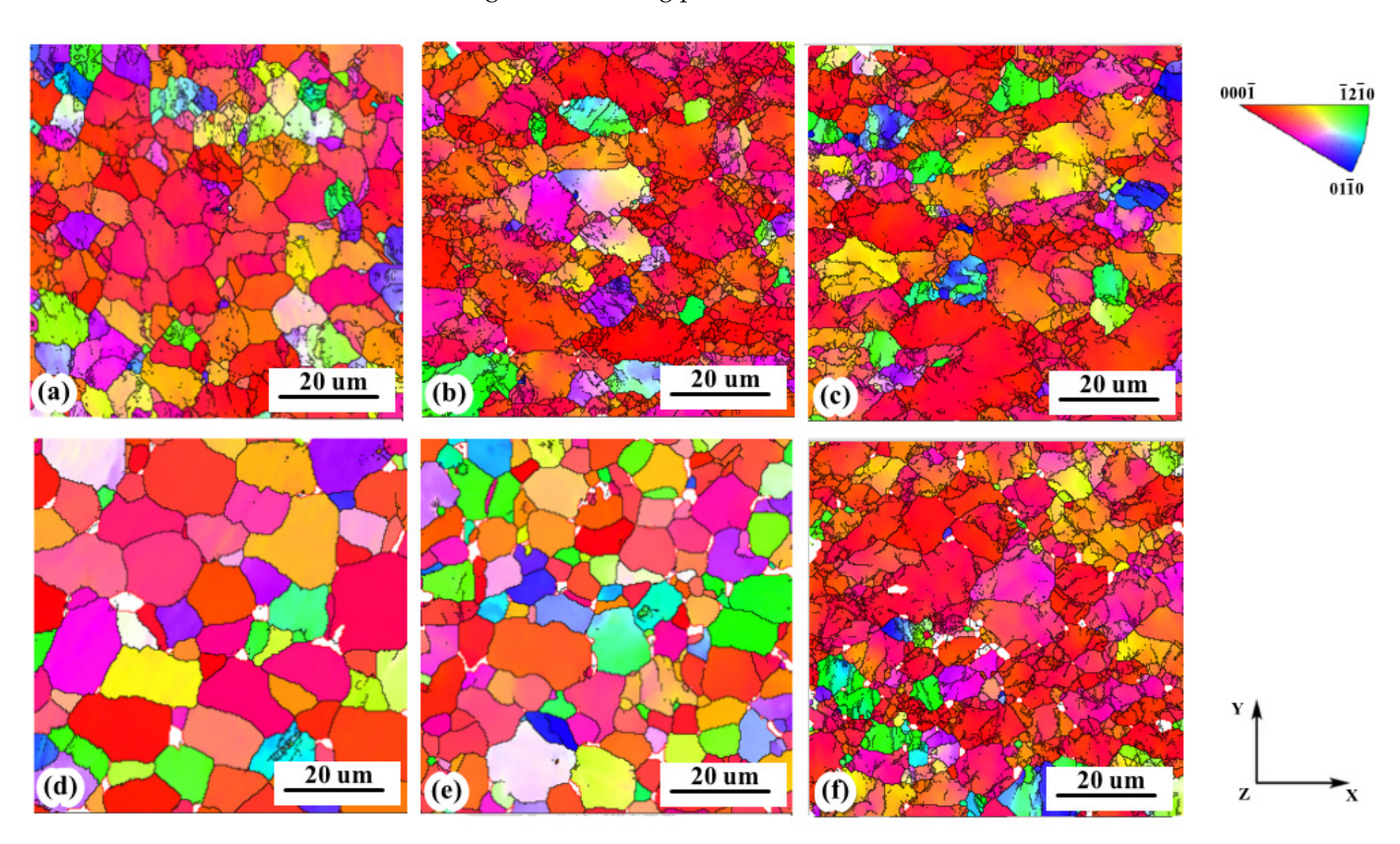


Figure 7. EBSD inverse pole figures at: (a) 930 °C, 10^{-2} /s; (b) 800 °C, 10^{-2} /s; (c) 600 °C, 10^{-2} /s; (d) 930 °C, 10^{-4} /s; (e) 800 °C, 10^{-4} /s; (f) 600 °C, 10^{-4} /s.

5. Conclusions

- (1) The investigations of the flow behavior of Ti-6Al-4V alloy after superplastic forming are given, and the emphasis is to discuss the deformability of the material during air cooling.
- (2) At $800\sim900$ °C and $10^{-4}\sim10^{-3}$ /s, the values of m are larger than 0.3, and the material has good deformability.
- (3) The evolution of deformation activation energy is influenced by dislocation movement.
- (4) The possibility of material damage gradually increases from 950 °C to 600 °C during air cooling.

Crystals **2022**, 12, 294 11 of 12

Author Contributions: X.H.: conceptualization, experimental investigations, programing, theoretical calculations, analysis, and writing—original draft. J.Y.: experimental investigations, discussion and review. J.L.: analysis, writing—review and editing, and supervision. J.W.: experimental investigations, discussion & review. All authors have read and agreed to the published version of the manuscript.

Funding: No funding supported this research.

Institutional Review Board Statement: Not applicable.

Informed Consent Statement: Not applicable.

Data Availability Statement: Not applicable.

Acknowledgments: The authors thank Northwestern Polytechnical University for providing the research infrastructure.

Conflicts of Interest: We declare that we have no financial or personal relationships with other people or organizations that could inappropriately influence our work, and there is no professional or other personal interest of any nature or kind in any product, service, and/or company that could be construed as influencing the position presented in, or the review of, the manuscript entitled, "Investigation of the flow behavior of air-cooling Ti-6Al-4V alloy after superplastic forming".

References

- 1. Agius, D.; Kourousis, K.I.; Wallbrink, C. A review of the as-built SLM Ti-6Al-4V mechanical properties towards achieving fatigue resistant designs. *Metals* **2018**, *8*, 75. [CrossRef]
- 2. Wu, T.; Wang, N.; Chen, M.; Zuo, D.; Xie, L.; Shi, W. Effect of pre-strain on microstructure and tensile properties of Ti-6al-4v at elevated temperature. *Metals* **2021**, *11*, 1321. [CrossRef]
- 3. Zhao, J.R.; Hung, F.Y.; Lui, T.S.; Wu, Y.L. The relationship of fracture mechanism between high temperature tensile mechanical properties and particle erosion resistance of selective laser melting Ti-6al-4v alloy. *Metals* **2019**, *9*, 501. [CrossRef]
- 4. Wu, M.W.; Chen, J.K.; Tsai, M.K.; Wang, S.H.; Lai, P.H. Intensification of preferred orientation in the additive manufactured Ti-6Al-4V alloy after heat treatment. *Mater. Lett.* **2021**, *286*, 129198. [CrossRef]
- 5. Geyer, M.; Vidal, V.; Pottier, T.; Boher, C.; Rézaï-Aria, F. Investigations on the material flow and the role of the resulting hooks on the mechanical behaviour of dissimilar friction stir welded Al2024-T3 to Ti-6Al-4V overlap joints. *J. Mater. Processing Technol.* **2021**, 292, 117057. [CrossRef]
- 6. Sun, Y.; Luo, G.; Zhang, J.; Wu, C.; Li, J.; Shen, Q.; Zhang, L. Phase transition, microstructure and mechanical properties of TC4 titanium alloy prepared by plasma activated sintering. *J. Alloy. Compd.* **2018**, 741, 918–926. [CrossRef]
- 7. Ratochka, I.; Lykova, O.; Mishin, I.; Naydenkin, E. Superplastic deformation behavior of Ti-4Al-2V alloy governed by its structure and precipitation phase evolution. *Mater. Sci. Eng. A* **2018**, 731, 577–582. [CrossRef]
- 8. Mosleh, A.; Mikhaylovskaya, A.; Kotov, A.; Pourcelot, T.; Aksenov, S.; Kwame, J.; Portnoy, V. Modelling of the superplastic deformation of the near-a titanium alloy (Ti-2.5AL-1.8MN) using arrhenius-type constitutive model and artificial neural network. *Metals* 2017, 7, 568. [CrossRef]
- 9. Mosleh, A.O.; Mikhaylovskaya, A.V.; Kotov, A.D.; Abushanab, W.S.; Moustafa, E.B.; Portnoy, V.K. Experimental investigation of the effect of temperature and strain rate on the superplastic deformation behavior of Ti-based alloys in the $(\alpha+\beta)$ temperature field. *Metals* **2018**, *8*, 819. [CrossRef]
- 10. Song, L.; Ii, A.; Despax, L.; Onishi, H.; Matsumoto, H.; Velay, V.; Vidal, V. Experimental analysis and behaviour modelling of the deformation mechanisms of a Ti-6242S alloy under hot and superplastic forming conditions. *Metals* **2020**, *10*, 1599. [CrossRef]
- 11. Mosleh, A.O.; Kotov, A.D.; Mestre-Rinn, P.; Mikhaylovskaya, A.V. Superplastic forming of Ti-4Al-3Mo-1V alloy: Flow behavior modelling and finite element simulation. *Procedia Manuf.* **2019**, *37*, 239–246. [CrossRef]
- 12. Velay, V.; Matsumoto, H.; Vidal, V.; Chiba, A. Behavior modeling and microstructural evolutions of Ti-6Al-4V alloy under hot forming conditions. *Int. J. Mech. Sci.* **2016**, *108*–109, 1–13. [CrossRef]
- 13. Alabort, E.; Kontis, P.; Barba, D.; Dragnevski, K.; Reed, R.C. On the mechanisms of superplasticity in Ti-6Al-4V. *Acta Mater.* **2016**, 105, 449–463. [CrossRef]
- 14. Ashby, M.F.; Verrall, R.A. Diffusion-accommodated flow and superplasticity. Acta Metall. 1973, 21, 149–163. [CrossRef]
- 15. Arieli, A.; Rosen, A. Superplastic deformation of Ti-6al-4v alloy. Met. Trans. A 1977, 8, 1591–1596. [CrossRef]
- 16. Zelin, M.G.; Mukherjee, A.K. Cooperative phenomena at grain boundaries during superplastic flow. *Acta Metall. Mater.* **1995**, 43, 2359–2372. [CrossRef]
- 17. Mochugovskiy, A.G.; Mikhaylovskaya, A.V.; Zadorognyy, M.Y.; Golovin, I.S. Effect of heat treatment on the grain size control, superplasticity, internal friction, and mechanical properties of zirconium-bearing aluminum-based alloy. *J. Alloy. Compd.* **2021**, 856, 157455. [CrossRef]
- 18. Rezaei, A.; Mahmudi, R.; Cayron, C.; Loge, R. Microstructural evolution and superplastic behavior of a fine-grained Mg–Gd–Y–Ag alloy processed by simple shear extrusion. *Mater. Sci. Eng. A* **2021**, *806*, 140803. [CrossRef]

Crystals **2022**, 12, 294

19. Alabort, E.; Barba, D.; Shagiev, M.R.; Murzinova, M.A.; Galeyev, R.M.; Valiakhmetov, O.R.; Aletdinov, A.F.; Reed, R.C. Alloys-by-design: Application to titanium alloys for optimal superplasticity. *Acta Mater.* **2019**, *178*, 275–287. [CrossRef]

- 20. Backofen, W.A.; Turner, I.R.A.D.H. Superplastic in an Al-Zn alloy. Trans. ASM 1964, 57, 980-990.
- 21. Alabort, E.; Putman, D.; Reed, R.C. Superplasticity in Ti-6Al-4V: Characterisation, modelling and applications. *Acta Mater.* **2015**, 95, 428–442. [CrossRef]
- 22. Zhang, R.; Shao, Z.; Lin, J. A review on modelling techniques for formability prediction of sheet metal forming. *Int. J. Lightweight Mater. Manuf.* **2018**, *1*, 115–125. [CrossRef]
- 23. Sun, P.; Wu, H.; Lee, W.; Shis, S.; Perng, J.; Lee, S. Cavitation behavior in superplastic 5083 Al alloy during multiaxial gas blow forming with lubrication. *Int. J. Mach. Tools Manuf.* **2009**, 49, 13–19. [CrossRef]
- 24. Huang, Y.; Langdon, T.G. Cavitation and failure in a fine-grained Inconel 718 alloy having potential superplastic properties. *Mater. Sci. Eng. A* **2005**, *410–411*, 130–133. [CrossRef]
- 25. Yang, J.; Wu, J.; Yang, D.; Wang, Q.; Wang, K.; Zhang, Z.; Wang, M.; Muzamil, M. A Modified Constitutive Model with Grain Rotation for Superplastic Forming of Ti-6Al-4V Alloy. *J. Eng. Mater. Technol. Trans. ASME* **2020**, 142, 1–13. [CrossRef]
- 26. Chen, L.; Zhao, G.; Yu, J.; Zhang, W. Constitutive analysis of homogenized 7005 aluminum alloy at evaluated temperature for extrusion process. *Mater. Des.* 2015, 66, 129–136. [CrossRef]
- 27. Quan, G.Z.; Luo, G.C.; Liang, J.T.; Wu, D.S.; Mao, A.; Liu, Q. Modelling for the dynamic recrystallization evolution of Ti-6Al-4V alloy in two-phase temperature range and a wide strain rate range. *Comput. Mater. Sci.* **2015**, *97*, 136–147. [CrossRef]
- 28. Wu, J.; Guo, R. Constitutive behavior for quenching of Al-Cu-Mg alloy with consideration of precipitation. *J. Eng. Mater. Technol. Trans. ASME* **2018**, 140. [CrossRef]
- 29. Zhao, S.; Zhang, H.; Cui, Z.; Chen, D.; Chen, Z. Superplastic behavior of an in-situ TiB2 particle reinforced aluminum matrix composite processed by elliptical cross-section torsion extrusion. *Mater. Charact.* **2021**, *178*, 111243. [CrossRef]
- 30. Kröhn, M.A.; Leen, S.B.; Hyde, T.H. A superplastic forming limit diagram concept for Ti-6Al-4V. *Proc. Inst. Mech. Eng. Part L J. Mater. Des. Appl.* 2007, 221, 251–264. [CrossRef]
- 31. Prasad, Y.V.R.K.; Gegel, H.L.; Doraivelu, S.M.; Malas, J.C.; Morgan, J.T.; Lark, K.A.; Barker, D.R. Modeling of dynamic material behavior in hot deformation: Forging of Ti-6242. *Metall. Trans. A* **1984**, *15*, 1883–1892. [CrossRef]
- 32. Gao, P.; Yu, C.; Fu, M.; Xing, L.; Zhan, M.; Guo, J. Formability enhancement in hot spinning of titanium alloy thin-walled tube via prediction and control of ductile fracture. *Chin. J. Aeronaut.* **2021**, *35*, 320–331. [CrossRef]